31st Congress of the International Council of the Aeronautical Sciences

Belo Horizonte, Brazil; September 09-14, 2018

FORCE FIGHT COMPENSATION FOR REDUNDANT ELECTRO-MECHANICAL FLIGHT CONTROL ACTUATORS

Robert Kowalski*, Jens Windelberg*, Raphael Ladner, Michael Rottach****

***German Aerospace Center (DLR e.V.) , ****Liebherr-Aerospace Lindenberg GmbH**

Keywords: *Electro-mechanical actuator, force fight, LQR, GRNN, actuator test rig*

Abstract

Electro-mechanical actuators (EMAs) for large civil aircraft require a nominal operation in active/active mode for certain primary flight control surfaces, like aileron and rudder, and thus measures to guarantee synchronous actuator movements. An approach for effective force fight compensation is introduced. It comprises a feedback loop designed as an optimal linear quadratic output regulator (LQR) and a feedforward controller based on a general regression neural network (GRNN). The implemented control scheme was validated on a test rig matching the physical properties of an aileron of a commercial single aisle aircraft.

1 Introduction

Power-by-Wire for flight control actuators is a promising solution to abolish heavy and badly accessible hydraulic piping and therefore having a benefit in production, maintenance and total system weight. EMAs are a key technology for that matter and e.g. already introduced at the trim horizontal stabilizer, the braking system and four spoilers of Boeing 787 [1].

To avoid single points of failure and improve reliability, aileron surfaces are mostly actuated in parallel redundancy while it is still open if hybrid or purely electro-mechanical actuation systems will dominate in future applications. Due to high reflected inertia the nominal operation in active/damping mode is not a favored solution for geared EMAs [2]. In active/active mode small deviations from the required actuator position Δx_{rod} result in a high undesired force fight ΔF between the actuators caused by a high attachment stiffness k:

$$\Delta F \approx k \cdot \Delta x_{rod} \tag{1}$$

In hybrid actuation systems consisting of an EMA, an electro-hydrostatic (EHA) and/or a conventional electro-hydraulic servo actuator (EHSA), force fight naturally occurs due to different actuator dynamics as investigated in [3] and [4]. Nevertheless, also in systems with nominally identical EMAs a force fight occurs resulting from system disturbances of various kinds [5], as marked in red in Fig. 1. This needs to be prevented by an active force fight compensation. An approach for the parallel-redundant operation of two aileron EMAs consisting of a feedback loop in conjunction with a neural feedforward controller is presented in this paper. In Chapter 2 a general linear system model is derived comprising the black elements in Fig. 1. Based on this model the feedback control in Chapter 3.1 is designed, marked with green lines in Fig. 1. The feedforward controller, described in Chapter 3.2, is marked with blue lines, while the temporary signal flow during the presented online learning procedure is marked with blue dotted lines.

The algorithms were validated on a test rig described in Chapter 4 with two aileron demonstrators shown in Fig. 2. The results of the validation and a conclusion are presented in Chapter 5 and 6.

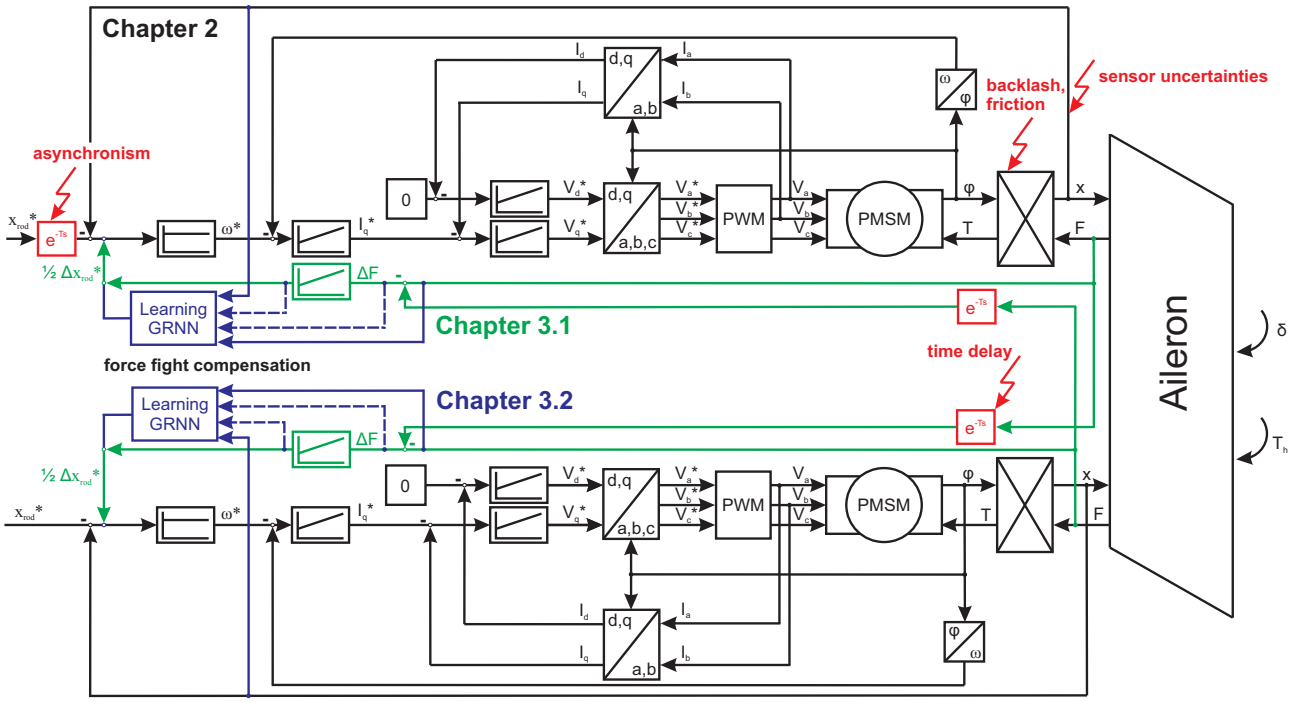

Fig. 1 Signal flow in the parallel-redundant aileron actuation system

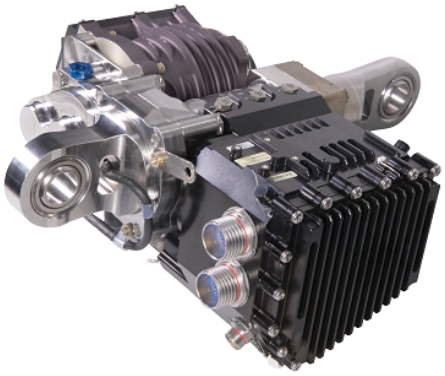

Fig. 2 Aileron EMA demonstrator from Liebherr-Aerospace utilized for validation tests

2 System Modelling

For the synthesis of a feedback force fight control, a complete state space model of the system was derived. It describes the powertrain of the EMAs consisting of a permanent magnet synchronous motor (PMSM), a reduction gear and a ball screw as well as a cascade position controller, the surface kinematics and attachments. A simplified model of the 3-phase motor was used covering the main dynamics of the PMSM. It is described in the d,q-rotor reference frame neglecting all current and voltage flow in direct axis I_d and V_d, considering an $I_d = 0$ control. Saliency effects mainly originating from the magnet layout on the rotor resulting in variable inductances in d- and q- direction are not addressed. Furthermore, saturation and temperature effects are not considered assuming a small effect on the outer position control loop. Therefore, the following 2-dimensional motor model was used:

$$\begin{pmatrix} \dot{I}_q \\ \ddot{\varphi} \end{pmatrix} = \begin{bmatrix} -\frac{R}{L} & -\frac{k_t}{L} \\ \frac{3}{2} \cdot \frac{k_t}{J} & 0 \end{bmatrix} \cdot \begin{pmatrix} I_q \\ \dot{\varphi} \end{pmatrix} + \ldots \\ \ldots \begin{bmatrix} \frac{1}{L} & 0 \\ 0 & -\frac{1}{J} \end{bmatrix} \cdot \begin{pmatrix} V_q \\ T_L \end{pmatrix} \tag{2}$$

with the stator winding resistance R, the quadrature axis inductance L, the motor constant k_t, the rotor inertia J, rotor angle φ and load torque T_L [6]. It is worth noticing that the generated torque is proportional to the current in quadrature axis:

$$T = \frac{3}{2} \cdot k_t \cdot I_q = \frac{3}{2} \cdot P \cdot \Psi_{PM} \cdot I_q \tag{3}$$

where the motor constant is the product of the number of pole pairs P and the permanent magnet flux Ψ_{PM}.

Gearboxes reduce the speed of the motor shaft by their reduction ratios i as shown in Eq. 4. At the same time they are assigned a generally high stiffness k_{GB} and a damping factor d_{GB} due to linearized viscous friction.

$$\begin{pmatrix} \dot{\varphi}_{in} \\ \ddot{\varphi}_{in} \\ \dot{\varphi}_{out} \\ \ddot{\varphi}_{out} \end{pmatrix} = \begin{bmatrix} 0 & 1 & 0 & 0 \\ -\frac{k_{GB}}{J_{in}} & -\frac{d_{GB}}{J_{in}} & \frac{k_{GB}\cdot i}{J_{in}} & \frac{d_{GB}\cdot i}{J_{in}} \\ 0 & 0 & 0 & 1 \\ \frac{k_{GB}}{J_{out}\cdot i} & \frac{d_{GB}}{J_{out}\cdot i} & -\frac{k_{GB}}{J_{out}} & -\frac{d_{GB}}{J_{out}} \end{bmatrix} \cdot \ldots \begin{pmatrix} \varphi_{in} \\ \dot{\varphi}_{in} \\ \varphi_{out} \\ \dot{\varphi}_{out} \end{pmatrix} + \begin{bmatrix} 0 & 0 \\ \frac{1}{J_{in}} & 0 \\ 0 & 0 \\ 0 & -\frac{1}{J_{out}} \end{bmatrix} \cdot \begin{pmatrix} T_{in} \\ T_{out} \end{pmatrix} \tag{4}$$

In order to further simplify the model, the reduction gear and the following ball screw were lumped to one generalized gearbox transforming all mechanical parameters to the motor side. For the purpose of the controller synthesis this is a reasonable assumption since the neglected eigenfrequencies are much higher than the bandwidths of the outer control loops.

The EMA is controlled in a conventional cascade control (see black elements in Fig. 1). The derivation of the control parameters K_{PC} and K_{IC} for the PI-current loop, K_{PS} and K_{IS} for the PI-speed loop and K_{PP} for the P-position loop are out of the scope of this paper. Nevertheless, the controllers were included in the general state space model (see Eq. 5) showing the dynamic response to a position reference value x^*_{rod}. The control errors of the speed and current controllers are e_s and e_c respectively and needed in order to include the integral action in the model.

The actuator is attached to the aileron by a simple hinge kinematics converting the linear motion into a rotation δ of the surface. It is characterized by an effective lever arm which is roughly identical to the geometrical lever length l at maximum deflection. The mechanical joints to the control surface and the wing structure were characterized by stiffness values k_s and k_h allowing the entire actuator with its mass m_h to slightly

$$\begin{bmatrix} e_S \\ e_C \end{bmatrix} = \begin{bmatrix} 0 & 0 \\ K_{IS} & 0 \end{bmatrix} \cdot \begin{bmatrix} \int e_S \\ \int e_C \end{bmatrix} + \begin{bmatrix} K_{PP} & 0 & -1 & -K_{PP} \\ K_{PS}\cdot K_{PP} & -1 & -K_{PS} & -K_{PS}\cdot K_{PP} \end{bmatrix} \begin{pmatrix} x^*_{rod} \\ I_q \\ \dot{\varphi} \\ x_{rod} \end{pmatrix}$$

$$V_q = \begin{bmatrix} K_{IS}\cdot K_{PC} & K_{IC} \end{bmatrix} \cdot \begin{bmatrix} \int e_S \\ \int e_C \end{bmatrix} + \begin{bmatrix} K_{PP}\cdot K_{PS}\cdot K_{PC} & -K_{PC} & -K_{PS}\cdot K_{PC} & -K_{PP}\cdot K_{PS}\cdot K_{PC} \end{bmatrix} \begin{pmatrix} x^*_{rod} \\ I_q \\ \dot{\varphi} \\ x_{rod} \end{pmatrix} \tag{5}$$

$$\begin{pmatrix} \dot{x}_h \\ \ddot{x}_h \\ \dot{\delta} \\ \ddot{\delta} \end{pmatrix} = \begin{bmatrix} 0 & 1 & 0 & 0 \\ -\frac{k_s+k_h}{m_h} & 0 & -\frac{k_s\cdot l}{m_h} & 0 \\ 0 & 0 & 0 & 1 \\ -\frac{k_s\cdot l}{J_s} & 0 & -\frac{2\cdot k_s\cdot l^2}{J_s} & 0 \end{bmatrix} \cdot \begin{pmatrix} x_h \\ \dot{x}_h \\ \delta \\ \dot{\delta} \end{pmatrix} + \begin{bmatrix} 0 & 0 \\ -\frac{k_s}{m_h} & 0 \\ 0 & 0 \\ -\frac{k_s\cdot l}{J_s} & \frac{1}{J_s} \end{bmatrix} \cdot \begin{pmatrix} x_{rod} \\ T_h \end{pmatrix}$$

$$F = \begin{bmatrix} k_s & 0 & k_s\cdot l & 0 \end{bmatrix} \cdot \begin{pmatrix} x_h \\ \dot{x}_h \\ \delta \\ \dot{\delta} \end{pmatrix} + \begin{bmatrix} k_s & 0 \end{bmatrix} \cdot \begin{pmatrix} x_{rod} \\ T_h \end{pmatrix} \tag{6}$$

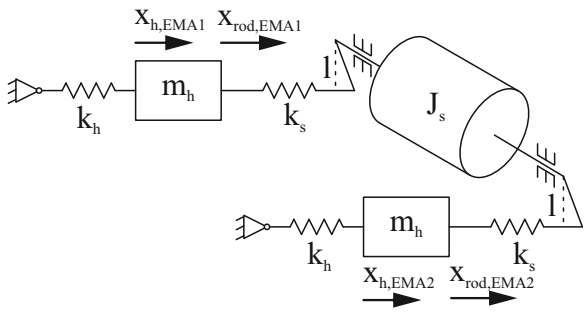

Fig. 3 Mechanical model of the actuation system

change its absolute position x_h in the wing. In addition to an external hinge moment T_h, the heavy surface inertia J_s needs to be accelerated to deflect the aileron. The mechanical system of Fig. 3 (neglecting all minor damping effects) is characterized by Eq. 6 resulting in the force F acting on the EMA output.

The conjunction of Eq. 2, 3, 4, 5 and 6 in one complete state space model fully describes the dynamics of a single EMA actuation system with a position reference input, a disturbing surface hinge moment and the resulting force on the actuator output.

For further investigation it is beneficial to rearrange Eq. 6 in two interconnected state space models for the actuator (see Eq. 7) and control surface dynamics (not shown) and to derive an actuator model from Eq. 2, 3, 4, 5 and 7.

$$\begin{aligned}\begin{pmatrix}\dot{x}_h\\ \ddot{x}_h\end{pmatrix} &= \begin{bmatrix}0 & 1\\ -\frac{k_s+k_h}{m_h} & 0\end{bmatrix}\cdot\begin{pmatrix}x_h\\ \dot{x}_h\end{pmatrix}+\ldots\\ &\ldots\begin{bmatrix}0 & 0\\ -\frac{k_s}{m_h} & -\frac{k_s\cdot l}{m_h}\end{bmatrix}\cdot\begin{pmatrix}x_{rod}\\ \delta\end{pmatrix}\\ F &= \begin{bmatrix}k_s & 0\end{bmatrix}\cdot\begin{pmatrix}x_h\\ \dot{x}_h\end{pmatrix}+\begin{bmatrix}k_s & k_s\cdot l\end{bmatrix}\cdot\begin{pmatrix}x_{rod}\\ \delta\end{pmatrix}\end{aligned} \tag{7}$$

In order to represent the force fight in a redundant actuation system the derived state spaces of both actuators are subtracted in Eq. 8.

$$\begin{aligned}\underline{\dot{x}_{EMA1}}-\underline{\dot{x}_{EMA2}} &= \underline{A}\cdot\ldots\\ \ldots(\underline{x_{EMA1}}-\underline{x_{EMA2}})+\underline{B}\cdot(\underline{u_{EMA1}}-\underline{u_{EMA2}})\\ y_{EMA1}-y_{EMA2} &= \underline{C}\cdot(\underline{x_{EMA1}}-\underline{x_{EMA2}})\end{aligned} \tag{8}$$

As both actuators have nominally the same dynamics a new state space representation can be derived, redefining the input, output and state vector as the difference between the inboard and outboard actuator. This 9-dimensional model constitutes the basis for the following control synthesis and has the general form:

$$\begin{aligned}\underline{\Delta\dot{x}} &= \underline{A}\cdot\underline{\Delta x}+\underline{B}\cdot\begin{pmatrix}\Delta x^*_{rod}\\ \Delta\delta\end{pmatrix}\\ \Delta F &= \underline{C}\cdot\underline{\Delta x}\end{aligned} \tag{9}$$

Assuming a rigid, non-twisting control surface, the disturbance due to an asymmetrical distribution of the hinge moment between the inboard and outboard actuators is neglected, leading to $\Delta\delta = 0$. The derived state space model 9 then describes how a non-equivalent position reference dynamically leads to a force fight at the actuator output. It is interesting to see that Eq. 9 is independent of the aileron kinematics described by its lever arm l, the surface inertia J_s and the external hinge moment T_h in this linear representation.

Examining Eq. 7 for the static case with all derivatives set to zero leads to the conclusion that the force fight is proportional to deviations in the actuator output position Δx_{rod} confirming the statement of Eq. 1:

$$\Delta F \approx \frac{k_s\cdot k_h}{k_s+k_h}\cdot\Delta x_{rod} \tag{10}$$

Note that this corresponds to the series connection of two ideal springs as shown in Fig. 3.

Furthermore it can be shown that state space 9 fulfills the properties of observability and controllability which is a condition for the following control synthesis.

3 Control synthesis

3.1 Feedback control

Since the force fight of the system predominantly depends on position deviations, a cascade control loop was chosen correcting the position reference values of the EMAs, as marked with green lines

in Fig. 1. The state space representation 9 allows to apply standard control synthesis methods for an active force fight control adjusting the reference inputs on the basis of force sensors at the output of the actuators. Naturally in most practical applications the force fight reference input ΔF^* would be zero to reject the unwanted asymmetrical load distribution on the actuation system.

A PI force feedback controller was used for dynamic and static force fight compensation. Therefore, the state space 9 was extended to Eq. 11 which defines, additionally to the force fight ΔF, the integral of the force fight $\int \Delta F dt$ as an output variable as well. This integral extension from [7] is a condition to allow integral action of the controller.

$$\begin{pmatrix} \underline{\Delta \dot{x}} \\ \Delta F \end{pmatrix} = \begin{bmatrix} \underline{A} & \underline{0} \\ \underline{C} & 0 \end{bmatrix} \cdot \begin{pmatrix} \underline{\Delta x} \\ \int \Delta F \end{pmatrix} + \begin{bmatrix} \underline{B} \\ 0 \end{bmatrix} \cdot \Delta x^*_{rod}$$
$$\begin{pmatrix} \Delta F \\ \int \Delta F \end{pmatrix} = \begin{bmatrix} \underline{C} & 0 \\ \underline{0} & 1 \end{bmatrix} \cdot \begin{pmatrix} \underline{\Delta x} \\ \int \Delta F \end{pmatrix} \tag{11}$$

For the controller synthesis an optimal linear quadratic output regulator (LQR) was designed from Eq. 11 according to [7] minimizing the cost function J_{cost} with the state vector $\underline{x}$, the control action u (here Δx^*_{rod}) and the weighting matrices $\underline{Q}$ and R.

$$J_{cost} = \int_0^\infty \underline{x(t)}^T \cdot \underline{Q} \cdot \underline{x(t)} + u(t)^T \cdot R \cdot u(t)\, \mathrm{d}t \tag{12}$$

The weighting matrices were chosen to be of the shape:

$$\underline{Q} = \underline{C}^T \cdot \begin{bmatrix} \rho_1 & 0 \\ 0 & \rho_2 \end{bmatrix} \cdot \underline{C}$$
$$R = \rho_3 \tag{13}$$

The tuning parameters ρ_1 and ρ_2 improve the rejection of the dynamic and the static force fight respectively, while ρ_3 emphasizes robust stability and reduced control effort. In systems with full state feedback the optimal controller that minimizes cost function 12 can be derived solving the well known Riccati-Equation. Nevertheless, for output controllers, the controller optimization by minimizing the cost function leads to three dependent optimality conditions with the unknown matrices $\underline{P}$, $\underline{L}$ and the controller matrix $\underline{K}$ [7].

$$\begin{aligned} (\underline{A} - \underline{BKC})^T \underline{P} + \underline{P}(\underline{A} - \underline{BKC}) + \ldots \\ \ldots \underline{C}^T \underline{K}^T R \underline{KC} + \underline{Q} = 0 \\ (\underline{A} - \underline{BKC})\underline{L} + \underline{L}(\underline{A} - \underline{BKC})^T + \underline{I} = 0 \\ \underline{K} = R^{-1} \underline{B}^T \underline{PLC}^T (\underline{CLC}^T)^{-1} \end{aligned} \tag{14}$$

The equations are solved iteratively to obtain the controller gains e.g. using the gradient descent method.

To confirm robust stability, the sensitivity to parameter uncertainties was analyzed. As shown in Fig. 4, special attention has to be paid to time delays reducing gain and phase margins of the force fight controller. This underlines the importance of a small latency in the bus communication between the electronic control units (ECU) of both EMAs.

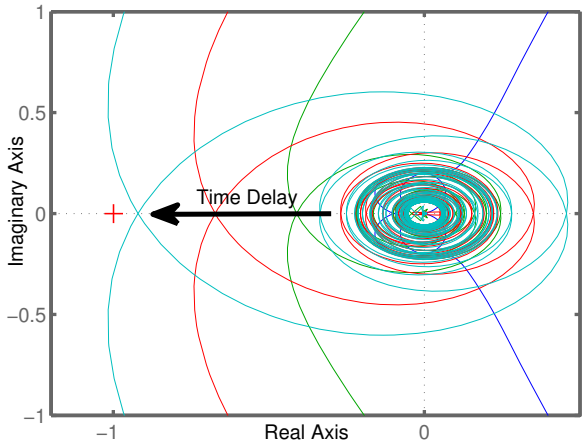

Fig. 4 Nyquist plot with varied time delays and its stability limit at (-1,0)

3.2 Neural feedforward control

The force fight between both actuators can be categorized into static and dynamic. While the dynamic part derives for the most part from slightly mismatching parameters of the plant, the static one results from measurement errors in the position determination of the LVDT (linear variable differential transformer), sensor calibration

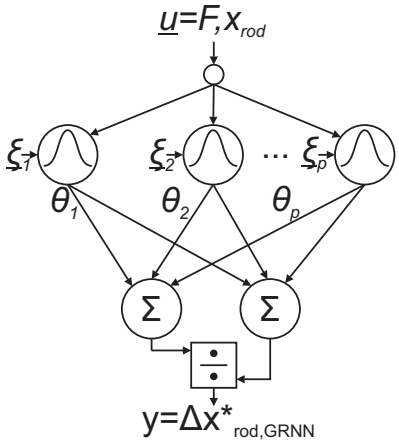

Fig. 5 General regression neural network

errors as well as geometric imperfections (within tolerances) from the production e.g. varying ballscrew pitch and installation process. The inherent backlash of the actuators combined with a high stiffness of the system contributes to a strong nonlinear behavior that depends on the stroke and the acting force on the actuators. As this results from imperfections that might be very different for each actuator, this nonlinearity is very hard to model or to identify with a classical parametric functions approach. But once the nonlinear relationship is known, it can be easily compensated. A good way to identify this nonlinearity for a given actuator is a simple neural network that is trained in an online fashion. The compensation will augment the PI force fight controller as marked with the blue elements in Fig. 1.

Since the feedforward control input (acting force F and measured stroke x_{rod}) and output (position compensation $\Delta x^*_{rod,GRNN}$) command dimensions are very small ([1x2] and [1x1] respectively) and the signal ranges are known, a general regression neural network (GRNN) was chosen as network architecture. The general structure of such a network, as described in [8], is depicted in Fig. 5.

In this single neuron layer network the range of each input is portioned into a 7-dimensional vector and for each of the $7 \cdot 7$ possible combinations of the vector values, a neuron is introduced into the network. The output of such a neuron is computed as a product of a weight parameter Θ_i and the so-called activation $\underline{A}$ of the neuron. The activation function is a Gaussian curve centered at the neuron position and evaluated with the squared Euclidian distance ξ_i of the network input to the neuron position. Three exemplary distances ξ_i are marked with black arrows in Fig. 6.

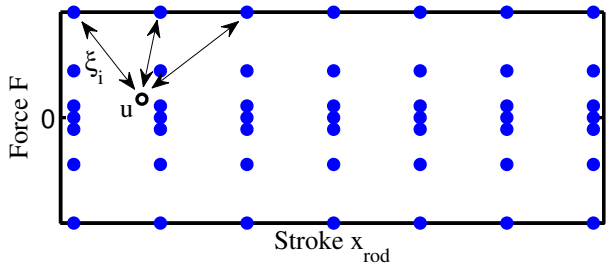

Fig. 6 Neurons of the GRNN

The output of all weighted neurons is summed and normalized by the sum of the activation of all neurons. To adapt the behavior of the network, the weights for each neuron are optimized. The optimization is done by minimizing the output error between a given set of measured input-output combinations and the network response with the same given inputs.

Because backlash will produce very steep force gradients in the region around $F = 0$, the neurons are not spread out evenly over the possible force range but rather more concentrated around $F = 0$ (see Fig. 6). This allows the reduction of the overall number of neurons without losing much accuracy and consequently the reduction of the computational efforts for the online training.

In the given structure (see Fig. 1) there is a dynamic system between output Δx^*_{rod} and input F, x_{rod} of the network. The EMA position dynamics introduce a phase shift between those signals. For training purposes, this phase shift needs to be accounted for as the network is only a static approximator and requires the input-output combination to have no delay. This compensation is done by an error transfer function $H(s)$ [8]:

$$H(s) = \underline{C}^T_{ff}(s\underline{I} - \underline{A}_{ff} + \underline{L}_{ff}\underline{C}^T_{ff})^{-1}\underline{B}_{ff} \qquad (15)$$

The compensation including a Luenberger

observer for the plant and a gradient descent training with learning rate η of the GRNN is achieved with the structure shown in Fig. 7 taken from [8].

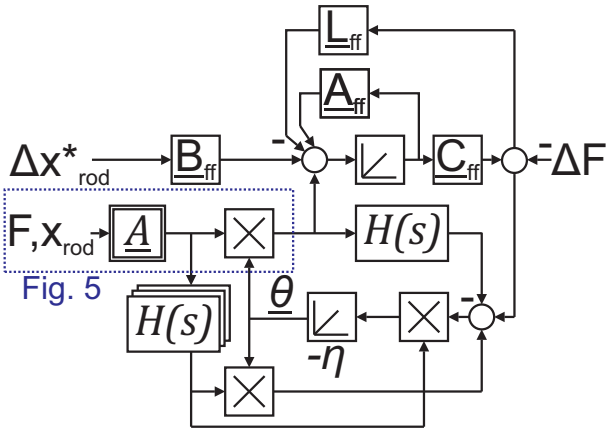

Fig. 7 State space observer with learning GRNN using gradient descent training

In the schematic, $\underline{A}_{ff}$, $\underline{B}_{ff}$ and $\underline{C}_{ff}$ represent the system matrix, the input and the output matrix of the reduced state space model 9, respectively. The observer gains $\underline{L}_{ff}$ are computed in a way to guarantee an asymptotical stable estimation error.

4 Test rig

The control scheme was validated on the flight control test rig shown in Fig. 8 with two redundant EMAs as shown in Fig. 2.

The physical properties of the aileron of a commercial single aisle aircraft according to Fig. 3 were matched. This includes the lumped attachment stiffness from Eq. 10, which was implemented with the spring element in Fig. 9. The correct stiffness was adjusted by the shape of the steel beam with its length l, width w, depth d, Young's modulus E and geometrical moment of inertia I [9] utilizing Eq. 16.

$$k = \frac{192 \cdot E \cdot I}{l^3} = \frac{16 \cdot E \cdot w \cdot d^3}{l^3} \qquad (16)$$

The aileron inertia J_s was matched with a mountable heavy disk attached to the aileron shaft. The junction between the EMAs and the aileron was accomplished with a hinge kinematics with the lever arm l. Representative hinge

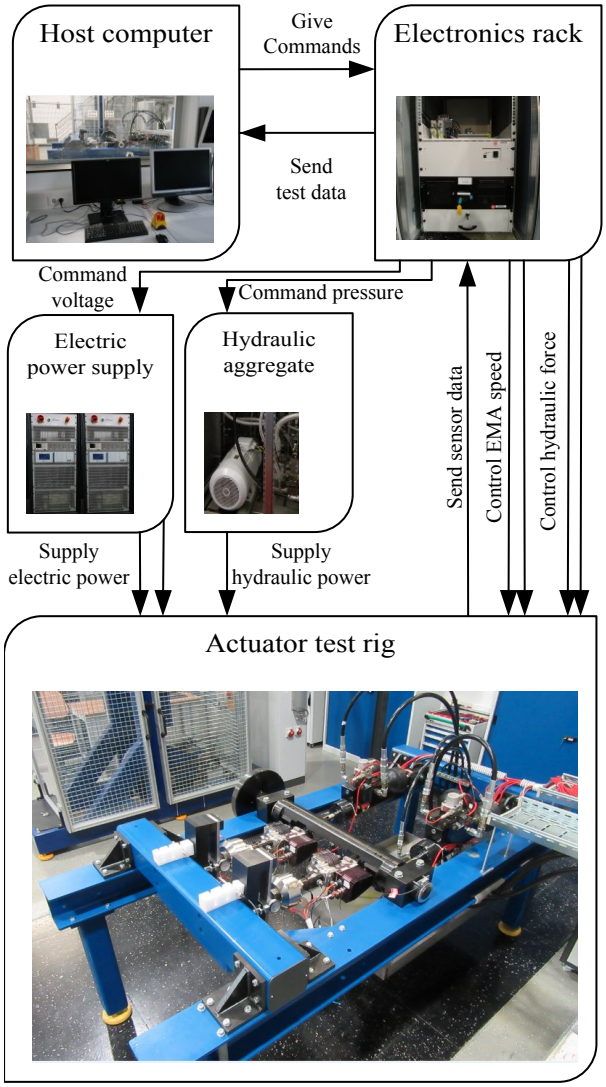

Fig. 8 Modular actuator test rig

moments were applied to the aileron shaft by two hydraulic servo actuators. In addition to internal EMA sensors used in position cascade control, external force sensors were applied providing the feedback to the force fight compensation. The test rig was supplied from an individ-

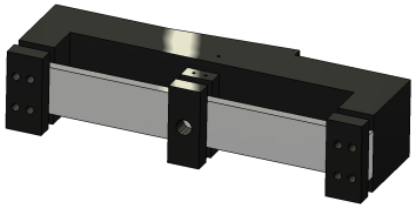

Fig. 9 Spring element design

ual DC power supply per EMA and a hydraulic power supply for the load actuators. The electronics rack comprises measuring amplifiers and a dSPACE real time computer. It includes among others the control algorithms of Chapter 3 and closes the position and force fight loops while the speed controllers are situated at the local ECUs of the EMAs. Furthermore, it contains the load control to apply variable hinge moments to the aileron. For that matter special attention had to be paid to compensate for varying effective lever arms of the hydraulic servo actuators due to the hinge kinematics. The test rig was controlled from a host PC with a GUI allowing the operation of the test rig in various modes with arbitrary position, load and force fight trajectories and the logging of the test data.

5 Validation

To demonstrate the presented control methods the feedback controller and the online learning algorithm were successively validated. Subsequently the performance of the combined algorithm including feedback and feedforward control was analysed. Finally the online learning algorithm was verified under varied mounting situations on the test rig introducing artificial backlash.

The optimal PI feedback controller from Chapter 3.1 was validated on the test rig by actively introducing a force fight into the test rig i.e. commanding a nonzero force fight reference trajectory ΔF^*. The frequency response to a chirp signal ΔF^* under a constant ordinary external lifting hinge moment T_h was measured. Fig. 10 shows a good matching between the closed loop state space model based on the physical EMA model from Chapter 2 and test data, confirming the assumptions of the design process. The predicted -3 dB bandwidth of the controller was confirmed.

An online learning procedure for the GRNN was performed to demonstrate the gradient descent method from Chapter 3.2. The trajectory in Fig. 11 was commanded on the test rig exciting the entire force range with the external hydraulic servo actuators and the entire stroke range

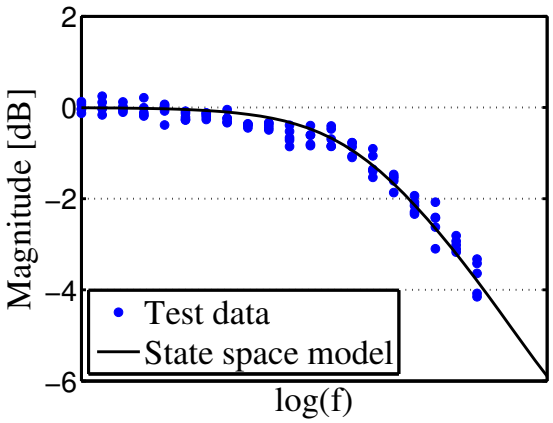

Fig. 10 Bode magnitude plot for active force fight control

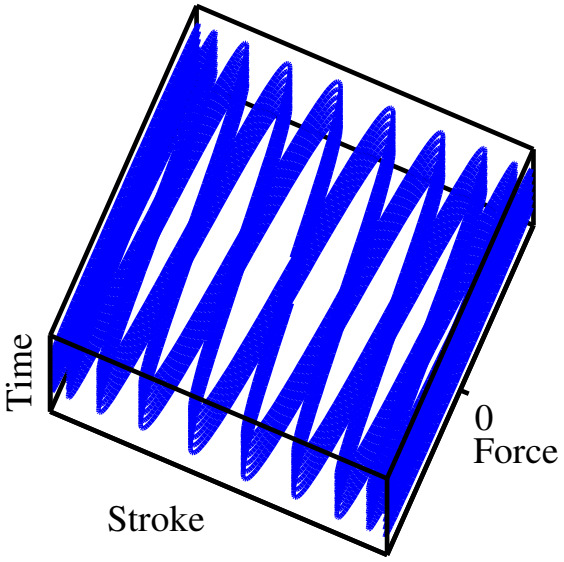

Fig. 11 Applied load and stroke trajectory for the online learning procedure

using EMA position control. It was performed with an enabled feedback force fight control to ensure compatibility with the learning algorithm.

The excited weights of the neurons of the GRNN as already shown in Fig. 6 showed a satisfying and stable convergence (see Fig. 12).

A nonlinearity curve as a function of EMA stroke and force representing the position mismatch at the actuator outputs was identified (see Fig. 13). A steep gradient at the transition between tensile and compressive forces indicates backlash in the attachments of the EMAs result-

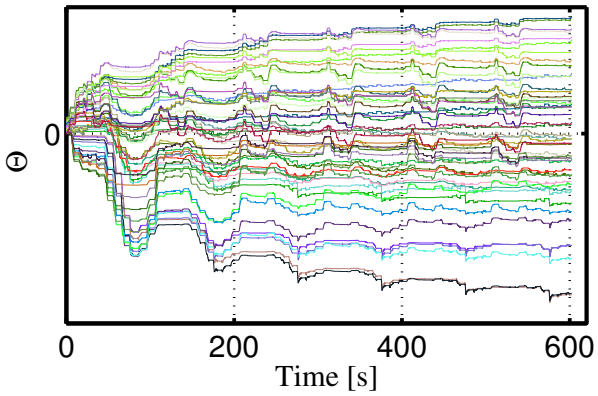

Fig. 12 Converging weight parameters of the neurons during online learning procedure

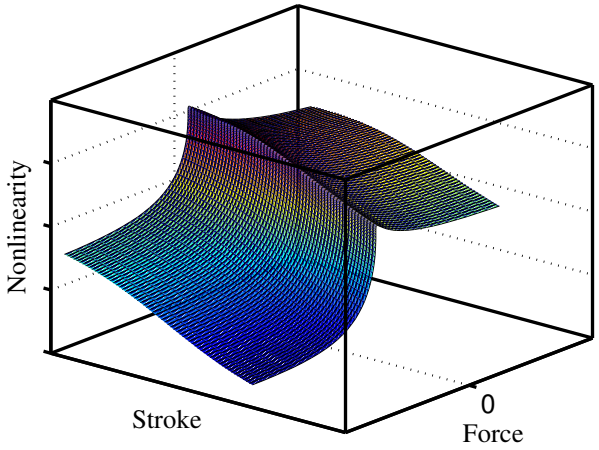

Fig. 13 Identified position mismatch at actuator outputs

ing in undesired force fight. Beside the dominant effect of backlash, geometrical manufacturing and mounting tolerances as well as LVDT measuring error cause deviations at different strokes.

The identified position mismatch was added to the position reference for compensation of static force fight. During the learning procedure, the action of the feedback controller declines continuously while the neural feedforward controller already compensates most disturbances. At the end of the presented learning procedure, the compensation is almost entirely transferred to the GRNN. This is shown in Fig. 14 where the crucial transition between tensile and compressive external loads is shown.

After successful demonstration of the joint operation of neural feedforward and PI feedback

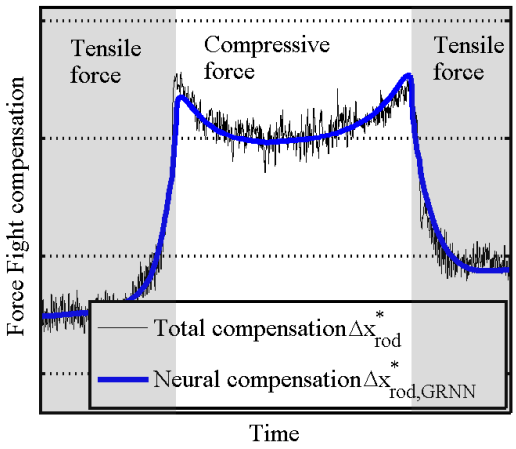

Fig. 14 Force fight compensation at the end of the online learning procedure

position compensation, the functionality of the method was verified under varied conditions. For this purpose, artificial backlash was introduced into the EMA attachments by mounting the actuators to the aileron shaft using loose running bolts with clearance fit. The learning algorithm quickly adopted to the new situation and adjusted its nonlinearity curve as shown in the set of curves in Fig. 15.

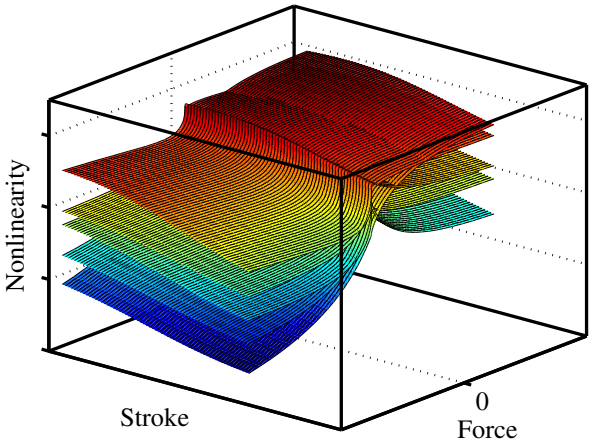

Fig. 15 Identified position mismatch at actuator outputs with varied backlash

6 Conclusion

A method for the synthesis of a force fight compensation for parallel-redundant primary flight

control actuators was presented. It consists of a PI-feedback controller which was designed solving optimality conditions according to the linear quadratic regulator (LQR) theory. Furthermore, a novel application of neural network feedforward control based on a GRNN was introduced improving the performance in the presence of backlash and geometrical uncertainties. The validation of the algorithms was performed on an aileron actuator test rig with two similar EMA demonstrators. A very good matching between the state space model and test data was accomplished showing the accuracy of the derived state space model. The neural feedforward control was successfully demonstrated showing its potential for future complex control tasks. It converged quickly during an online learning procedure using the gradient descent method to train the neurons of the network. In the future it would be desirable to further extend the neural network to compensate for dynamic force fight correlated to speed and acceleration of the EMAs as well.

References

[1] Maré J-C. *Aerospace Actuators 2*. 1st edition, ISTE Ltd, 2017.

[2] Arriola D and Thielecke F. Design of Fault-Tolerant Control Functions for a Primary Flight Control System with Electromechanical Actuators. *IEEE AUTOTESTCON*, National Harbor, pp. 393-402, 2015.

[3] Cochoy O. *Investigation for the Synchronized Operation of a Hybrid Actuator Configuration in Redundant Flight Control Systems*. Shaker Verlag, 2009.

[4] Röben T, Stumpf E, Grom T and Weber G. An innovative all-active hybrid actuation system demonstrator. *International Workshop on Aircraft System Technologies*, Hamburg, 2017.

[5] Kowalski R. Force Fight in Parallel-Redundant Electro-Mechanical Actuation Systems. *Proceedings of More Electric Aircraft*, Bordeaux, 2017.

[6] Isermann R. *Mechatronische Systeme*. 2nd edition, Springer, 2008.

[7] Lunze J. *Regelungstechnik 2*. 4th edition, Springer, pp 144-145, pp 307-311, 2006.

[8] Schröder D. *Identifikation und Regelung nichtlinearer Systeme*. 1st edition, Springer, pp 48-58, pp 127-139, 2010.

[9] Paland, E-G. *Technisches Taschenbuch*. 7th edition, Schaeffler KG, 2002.

7 Contact Author Email Address

robert.kowalski@dlr.de

8 Acknowledgment

This work was supported by the German Federal Ministry for Economic Affairs and Energy (BMWi) in the framework of the Federal Aeronautical Research Program (LuFo V-1 EMA PFC Subsystem under the support code 20Y1304B).

Copyright Statement